ADVANCED ELECTRONIC MATERIALS
www.advelectronicmat.de

Numerical Device Model for Organic Light-Emitting Diodes Based on Thermally Activated Delayed Fluorescence

*Bas van der Zee, Yungui Li, Gert-Jan A. H. Wetzelaer, and Paul W. M. Blom**

In organic light-emitting diodes (OLEDs) based on thermally activated delayed fluorescence (TADF), non-emissive triplet excitons are converted to emissive singlet excitons via reverse intersystem crossing (rISC). To model the operation of TADF-based OLEDs, quantification of the triplet population is therefore a prerequisite. A numerical drift-diffusion model is presented for TADF OLEDs that next to singlet and triplet generation also includes the positional dependence of intersystem crossing, rISC and triplet-triplet annihilation (TTA). As experimental model system, a single-layer OLED is used based on the TADF emitter 9,10-bis(4-(9H-carbazol-9-yl)–2,6-dimethylphenyl)–9,10-diboraanthracene that possesses nearly trap-free transport and a high photoluminescence quantum yield. The model accurately describes the voltage dependence of the current density and external quantum efficiency (EQE), both as a function of temperature and active layer thickness. The model reveals that the steep increase in EQE at low voltage originates from emissive trap states, whereas the efficiency decrease at high voltage is dominated by TTA, with a temperature independent rate constant of $7 \pm 3 \times 10^{-18}$ m^3 s^{-1}. The model allows us to quantitatively disentangle the various contributions of direct and trap-assisted recombination as well as recombination following rISC to the EQE, providing a useful tool for further optimization of TADF OLEDs.

1. Introduction

Commercial organic light-emitting diodes (OLEDs) typically make use of phosphorescent molecules to generate electroluminescence (EL). The strong spin-orbit coupling of the heavy-metal complexes enables the harvesting of both singlet and triplet excitons under electrical excitation, which cannot be realized with conventional fluorescent emitters, leading to unprecedented internal and external quantum efficiencies (IQE/EQE).[1,2] A multilayer architecture is generally needed to attain these high EQEs, where the several layers aid in injection, transport, light generation, and blocking of charges and/or excitons. Phosphorescent OLEDs also have the drawback of using expensive, environmentally unfriendly heavy-metal complexes. In 2012, a new class of fully organic OLED materials emerged using thermally activated delayed fluorescence (TADF).[3,4] Here, the small singlet-triplet energy gap allows for efficient conversion from triplets to singlets on the same molecule, i.e., efficient reverse intersystem crossing (rISC) prompted by thermal energy. Therefore, while retaining the theoretically achievable 100% IQE, the necessity of an added toxic heavy-metal element was eliminated. Consequently, TADF materials are being treated as promising candidates for highly efficient OLEDs and have therefore gained considerable scientific attention in recent years.[5–8] High efficiencies have been demonstrated for TADF devices employing host–guest systems in multilayer architectures, similar to phosphorescent OLEDs. However, due to the many variables induced by multilayer architectures, such as the individual transport properties of the layers and ill-defined barriers at the heterojunctions, a quantitative understanding of the device operation of TADF OLEDs is hampered. For this reason, a comprehensive device model for TADF OLEDs is presently lacking. In contrast, single-layer polymer LEDs (PLEDs) have been successfully modeled with a well-established numerical drift-diffusion simulation program.[9–12] Also for TADF OLEDs, a simplified device structure would strongly benefit the development of a quantitative device model for TADF OLEDs.

Recently, an efficient TADF OLED (EQE ≈ 19% at 500 cd A^{-1}) was demonstrated based on a single TADF emitting layer of pristine 9,10-bis(4-(9H-carbazol-9-yl)–2,6-dimethylphenyl)–9,10-diboraanthracene (CzDBA),[13] of which the chemical structure is shown in **Figure 1**a. A photoluminescence quantum yield (PLQY) of >90% in the neat film, low electron- and hole-trap densities combined with balanced bipolar transport[14] and efficient charge injection via Ohmic electron and hole contacts,[15] make these single-layer CzDBA OLEDs an ideal model system to uncover the device physics of OLEDs based on TADF emitters. In a recent study, the efficiency decrease at high voltage (roll-off) of a single-layer CzDBA OLED was studied using analytical formulas,[16] and triplet–triplet annihilation (TTA) was identified to be the origin of the roll-off in EQE at high voltages. However, in this analytical approach a number of assumptions were made by neglecting the following features: the effect of intersystem crossing (ISC), the effect that TTA generates singlets,

---

B. van der Zee, Y. Li, G.-J. A. H. Wetzelaer, P. W. M. Blom
Max Planck Institute for Polymer Research
Ackermannweg 10, 55128 Mainz, Germany
E-mail: blom@mpip-mainz.mpg.de

The ORCID identification number(s) for the author(s) of this article can be found under https://doi.org/10.1002/aelm.202101261.

DOI: 10.1002/aelm.202101261

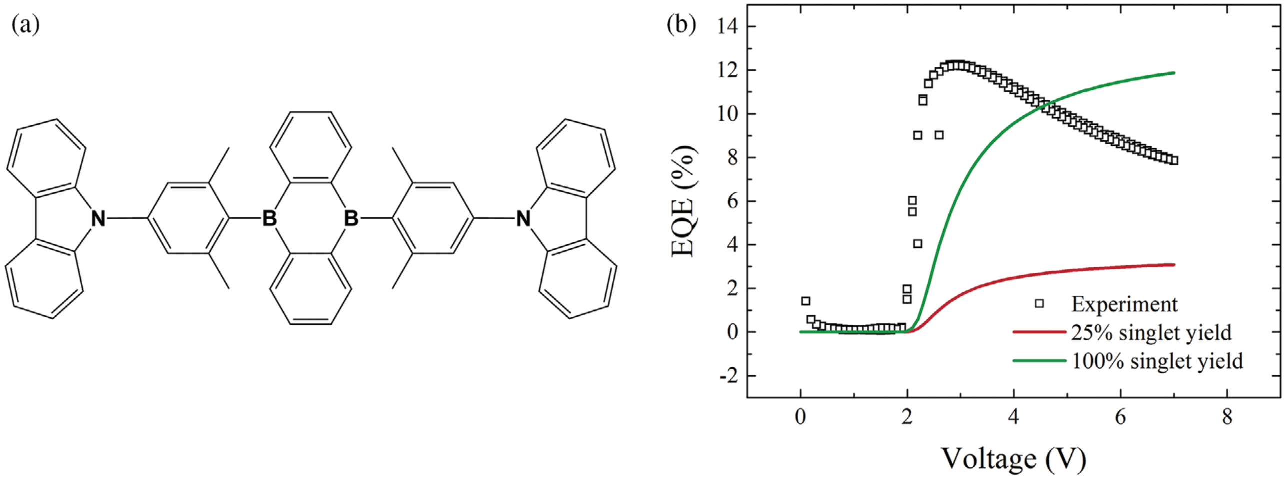

Figure 1. a) Chemical structure of CzDBA. b) Experimental external quantum efficiency versus voltage for a CzDBA OLED with an active-layer thickness of 200 nm (black symbols) and the simulated efficiencies (solid lines) for a 25% singlet yield (conventional fluorescent emitter) and a 100% singlet yield (TADF emitter), excluding excitonic interactions.

the monomolecular decay of triplets, and the positional dependence of numerous quantities, such as bimolecular and trap-assisted charge recombination, in the device. Most importantly, although an analytical approach can provide insight into a specific aspect, such as the origin of the efficiency roll-off, it does not provide a full quantitative description of the efficiency and device operation of TADF OLEDs. In this study, we integrate all the previously neglected processes and features in a numerical device model in order to elucidate the TADF OLED device physics and quantitatively describe the various contributions to the quantum efficiency. First, we discuss how the existing single-layer PLED device model with a position-dependent exciton generation rate is expanded with the rate equations for singlet and triplet excitons to include forward and reverse intersystem crossing rates, as well as annihilation processes as TTA, triplet-polaron quenching (TPQ) and singlet-triplet annihilation (STA). As a next step, the model is applied to single-layer CzDBA OLEDs to describe the temperature-dependent current density and external quantum efficiency for a range of active layer thicknesses. We demonstrate that the high EQE at low voltages originates from the fact that recombination via traps in CzDBA is emissive, in contrast to the nonradiative trap-assisted recombination typically observed in PLEDs. The roll-off of the efficiency at higher voltages is well described by the TTA process at all temperatures with a rate constant of $7 \pm 3 \times 10^{-18}$ m^3 s^{-1}. It is furthermore demonstrated that the efficiency roll-off can be attributed to TTA and that the incorporation of other annihilation processes like TPQ and STA cannot reproduce the experiment. Finally, the model enables us to break down the several contributions to the OLED efficiency in a quantitative way. The availability of the presented comprehensive device model will greatly aid the further development of TADF OLEDs.

2. Results and Discussion

2.1. Fluorescent Drift-Diffusion Model

In this work, the *J–V* characteristics are modeled using numerical drift-diffusion simulations, with the field-, density-, and temperature-dependence of the mobility being described by the extended Gaussian disorder model (EGDM).[17] Such simulations were successfully employed to model the *J–V* characteristics of fluorescent PLEDs.[9–12] In the simulation program, the Poisson and continuity equations are solved in a position-dependent fashion to obtain the carrier density in the device: n for electron density, p for hole density. The mobility (μ) in the EGDM is then given by a density-dependent mobility, for n and p separately, multiplied by a field-dependent function (f):

$$\mu(T,p,E) = \mu(T,p) \times f(T,E) \tag{1a}$$

where

$$\mu(T,p) = \mu_0 \exp\left[-0.42\hat{\sigma}^2 + \frac{1}{2}\left(\hat{\sigma}^2 - \hat{\sigma}\right)\left(2pa^3\right)^{\delta}\right] \tag{1b}$$

$$f(T,E) = \exp\left[0.44\left(\hat{\sigma}^{3/2} - 2.2\right) \times \sqrt{1 + 0.8\left(\frac{Eea}{\sigma}\right)^2} - 1\right] \tag{1c}$$

with

$$\delta = \frac{2\ln\left(\hat{\sigma}^2 - \hat{\sigma}\right) - 2\ln(\ln 4)}{\hat{\sigma}^2} \tag{1d}$$

$$\hat{\sigma} = \frac{\sigma}{k_B T} \tag{1e}$$

The same equations are used for the electron density by replacing p with n. Here, the fit parameters are the zero-field mobility μ_0 [m^2 V^{-1} s^{-1}], the average hopping distance a [m], and the width of the Gaussian density of states (DOS) σ [eV]. Additional simulation parameters are given in the methods section. As a first step towards the modeling of the TADF OLED, the charge transport properties of the electrons and holes need to be investigated separately. The density-, field-, and temperature-dependent mobility can be obtained by fitting the current-density voltage characteristics of single-carrier devices, i.e., hole-only (HO) and electron-only (EO) devices.[18] In an earlier

Table 1. Simulation parameters for the electron- and hole-only devices, the *e*/*h* superscripts refer to the parameter being for electrons/holes respectively. N_t/P_t is the electron/hole trap density, which is located at a trap depth E_{Nt}/E_{Pt} below the middle of the density-of-states of states of the material, with a width of $\sigma_{Nt/Pt}$.

Charge-transport parameters	Value
μ_0^e	5000 m^2 V^{-1} s^{-1}
μ_0^h	20 000 m^2 V^{-1} s^{-1}
a^e	1.5×10^{-9} m
a^h	1.3×10^{-9} m
σ^e	0.115 eV
σ^h	0.135 eV
N_t	1.4×10^{22} m^{-3}
P_t	1.7×10^{22} m^{-3}
$E_{N_t} = E_{P_t}$	0.65 eV
$\sigma_{N_t} = \sigma_{P_t}$	0.1 eV

study, the HO and EO devices of CzDBA were successfully modeled,[14] from which the obtained charge transport parameters are presented in **Table 1**. The traps that were added follow a Gaussian distribution, like the density of states itself, and therefore also carry a certain σ.

The measured room temperature mobilities of the electrons and holes are well balanced, being $\mu_e = 5 \times 10^{-5}$ cm^2 V^{-1} s^{-1} and $\mu_h = 3 \times 10^{-5}$ cm^2 V^{-1} s^{-1}, respectively. Furthermore, with an ionization energy of 5.9 eV and electron affinity of 3.5 eV, the energy levels of CzDBA are located inside the energy window for trap-free charge transport in organic semiconductors.[19] However, as shown in Table 1, the electron and hole transport is not completely trap free, but the obtained trap density of $\approx 10^{22}$ m^{-3} is typically an order of magnitude lower than for the universal traps that are attributed to oxygen and/or water complexes, for which the density is in the 10^{23} m^{-3} regime. With the electron and hole transport parameters known, the CzDBA OLED can be modeled. As an intermediate step, we calculate the efficiency of a conventional fluorescent OLED,[9] using the charge-transport parameters obtained for CzDBA. For the light output, we consider the Langevin recombination rate (R_L) as well as the trap-assisted Shockley-Read-Hall (SRH) rate (R_{SRH}). These are related to the mobility and charge-carrier density as follows:

$$R_L = \frac{e}{\varepsilon_0 \varepsilon_r}\left(\mu_p + \mu_e\right) np \tag{2a}$$

$$R_{\mathrm{SRH}} = \frac{C_n C_p N_t}{C_n\left(n+n_1\right)+C_p\left(p+p_1\right)}\left(np - n_1 p_1\right) \tag{2b}$$

where n_1/p_1 are the equilibrium electron/hole densities. The capture coefficient ($C_{n/p}$) is given by

$$C_{n/p} = \frac{q}{\varepsilon}\mu_{n/p} \tag{2c}$$

We note that since the electron density $n(x)$ and hole density $p(x)$ are position-dependent also the Langevin and SRH recombination rates are position-dependent. For fluorescent LEDs we take the local Langevin recombination rate $R_L(x)$ as the generation rate $G(x,t)$ for excitons and without the addition of further processes this is related to the local emissive singlet density $[S(x,t)]$ as $[S(x,t)] = 0.25G(x,t) \cdot \tau_s$, with τ_s the singlet exciton lifetime. The total light output is then obtained by integrating the local emissive recombination rate of $0.25G(x,t)$ over the device thickness. This leads to the conventional "fluorescent" efficiency in Figure 1b as the red line, while the experimental efficiency of a 200 nm CzDBA OLED at room temperature is shown as black symbols. The CzDBA OLED is essentially a single-layer device, with a neat film of CzDBA sandwiched between Ohmic electron and hole contacts. The fabrication and full device structure of these single-layer CzDBA OLEDs was outlined previously.[13] We observe that the predictions of the model strongly deviate from the experimental efficiency, most notably the simulation underestimates the efficiency and the voltage dependence does not match the experiment. The reason for the too low-efficiency values is straightforward: fluorescent models assume that only 25% of the generated excitons contributes to the light output, explaining the approximate factor 3 between the maximum of the experiment and the maximum calculated efficiency (red line). Therefore, as a next step, the exciton dynamics appropriate to TADF should be taken into account.

2.2. TADF Model

For this purpose, rate equations are a well-known approach and have been applied previously to study photoluminescence (PL) and EL transients as well as investigate the efficiency of TADF devices.[16,20,21] Rate equations for the singlet $[S(x,t)]$ and triplet $[T(x,t)]$ density take the form of linear differential equations:

$$\begin{aligned}\frac{d\left[S(x,t)\right]}{dt} = {} & 0.25 \cdot G(x,t) - \frac{\left[S(x,t)\right]}{\tau_s} + k_{rISC} \cdot \left[T(x,t)\right] \\ & - k_{ISC} \cdot \left[S(x,t)\right]\end{aligned} \tag{3}$$

$$\begin{aligned}\frac{d\left[T(x,t)\right]}{dt} = {} & 0.75 \cdot G(x,t) - \frac{\left[T(x,t)\right]}{\tau_t} - k_{rISC} \cdot \left[T(x,t)\right] \\ & + k_{ISC} \cdot \left[S(x,t)\right]\end{aligned} \tag{4}$$

where $G(x,t)$ [m^{-3} s^{-1}] is the local generation rate incorporating R_L, $k_{(r)\mathrm{ISC}}$ [s^{-1}] the (reverse) intersystem crossing rate and $\tau_{s/t}$ [s] the singlet/triplet lifetime. Quantities denoted as a function of x are taken as position-dependent quantities in the simulations, whereas t denotes a time dependence.

We note that both the rate equations assume that there is only one relevant excited singlet and triplet level. Together with the singlet ground state, one arrives at a model with three relevant energy levels. As reports from different groups have pointed out,[22,23] a small singlet-triplet gap only partly explains an efficient spin flip between two charge transfer (CT) states. The spin-orbit coupling must be considered as well and therefore the importance of a triplet locally excited state (^{3}LE) in rISC was recognized. For example, a four-level model, where a higher lying triplet state was included, has been used to explain the photo physics of TADF emitters previously.[24] Omitting LE singlet levels on the one hand is justified by the fact that they generally vanish after ≈5 ns,[25] a consequence of the fact that their locally excited nature does not allow them to be repopulated via rISC. The light output that originates from LE singlets in steady state will thus be negligible compared to the contribution from the fluorescence of CT singlets. LE triplet states on the other hand have been shown to mix efficiently with CT triplet states, making it possible to consider one effective triplet level coupled to the singlet state through an effective k_{rISC}.[25] Furthermore, it has been shown that efficient TADF is obtained between mixed singlet and triplet states with different CT/LE contributions.[26] The exact electronic character (CT, LE, or mixed) of the triplet is therefore not of relevance in our device model, and whereas in reality a spin flip proceeds via a local intermediate energy state, a three-level model embeds the salient features of TADF photophysics and can therefore be reliably employed.

The rate equations can be solved in steady state to obtain $[S(x)]$ and $[T(x)]$ at every voltage, using values for $k_{\mathrm{(r)ISC}}$ and other photophysical parameters published previously,[27] but for completeness we present them here again in **Table 2**. The steady-state local singlet concentration $[S(x)]$, as derived in Section 1 of the Supporting Information, is given by

$$[S(x)] = \frac{0.25 \cdot G(x) + [T(x)] \cdot k_{rISC}}{\tau_s^{-1} + k_{ISC}} \tag{5}$$

Whereas the derivation of the local triplet density $[T(x)]$ can be found in Supporting Information Section 1.

Incorporation of the exciton dynamics in the TADF OLED device model is done by using the local triplet concentration to obtain the singlet concentration (Equation 5). The exciton density is divided by τ_s to obtain the recombination rate, which after integration over the device thickness and dividing by the number of electrical charges per unit time J/q gives the internal quantum efficiency. Experimentally, the EQE of 19% for an 80 nm device is reduced to around 12% for a 200 nm device, as a result of the nonideal optical cavity, reducing the outcoupling efficiency.[28] Taking into account the forward and reverse intersystem crossing, as well as the optical outcoupling efficiency, we arrive at the simulated green line in Figure 1b, which now reaches the maximum observed experimental EQE, but we still observe a discrepancy between experiment and theory over the whole voltage range. For voltages just above the built-in voltage (V_{bi}), the experimental EQE increases much faster than the predicted green line. Studies on PLEDs have shown that trap-limited transport causes a competition between nonradiative trap-assisted SRH and radiative Langevin-type bimolecular recombination, where the stronger scaling with charge density of the latter leads to a rise and ultimately a plateau in the efficiency as a function of voltage.[29] Using the trapping parameters obtained from single-carrier devices, the green line indeed displays this behavior, whereas the experimental efficiency increases in an almost vertical fashion just after V_{bi}, a situation that typically occurs when (almost) no traps are present in the material. These apparently conflicting findings can be reconciled by assuming that the majority of the trap states in CzDBA are emissive. As a first indication that CzDBA contains light-emitting traps we show that these traps can be differentiated from the main fluorescence peak in a PL spectrum. In Figure S1 (Supporting Information) we de-convoluted the PL spectrum into several Gaussian peaks.[30–32] The PL spectrum is asymmetric, exhibiting a broad Gaussian profile with a maximum located 0.65 eV below the middle of the main fluorescence peak. This corresponds exactly to the energy difference between the middle of the material DOS and the middle of the trap DOS found from single-carrier devices (Table 1) and therefore we assign this lower-energy part of the spectrum to emissive recombination via trap states. As a second indication that emissive trap-assisted recombination takes place, we calculated the ideality factor η_L of the luminance using the equation $\eta_L = \left(\frac{k_B T}{q}\frac{\partial \ln L}{\partial \ln V}\right)^{-1}$. The ideality factor can indicate the type of recombination, as it amounts to 1 for bimolecular and up to 2 for Shockley-Read-Hall (SRH) recombination.[29] A plot of the ideality factor can be found in Figure S2, Supporting Information, where we extract the ideality factor from the plateau value. We observe that η_L exceeds 1 (≈ 1.5), meaning that a substantial part of the light-output in this voltage regime stems from trap-assisted recombination. In the simulation, we therefore included that SRH-recombination contributes to the light output, by incorporating R_L as well as R_{SRH} into $G(x,t)$, leading to a steep increase of the efficiency with voltage. Although the exact origin of these traps is currently unknown, we speculate that on a molecular level these traps could correspond to aggregates or molecules with different molecular conformations with lower bandgap, as these could act as electrical trap states, but since the molecules would still be intact, they can also emit light. This would also explain that in spite of the CzDBA energy levels being in the trap-free energy window with regard to oxygen/water trapping, there is still a low trap concentration present with traps of a different origin.

As a next step, we now address the mismatch between the calculated green line (Figure 1b) and the experiment at higher voltage. A longstanding problem for the efficiency of both phosphorescent and TADF OLEDs is their efficiency decrease (roll-off) with increasing voltage, and thus brightness. Several mechanisms for explaining the origin of the roll-off have been suggested, including triplet-triplet annihilation (TTA),[33–36] triplet-polaron quenching (TPQ)[35] and singlet-triplet annihilation (STA).[20,37] Here, we will first focus on TTA, as it was reported to be the dominant roll-off mechanism in CzDBA OLEDs following an analytical approach.[16] A discussion of the

Table 2. Photophysical parameters obtained from the photoluminescence decay of CzDBA,[27] as used in the simulation.

Photophysical parameters	Value
k_{ISC}	1×10^6 s^{-1}
k_{rISC}	2.2×10^5 s^{-1}
ΔE_{ST}	33 meV
τ_s	98 ns
τ_t	100 µs[a]

[a] Note that the exact value of the triplet lifetime is unknown, but we take it to be sufficiently long such that phosphorescence becomes a negligible process, as it should be in the temperature range we are considering (295–215 K).

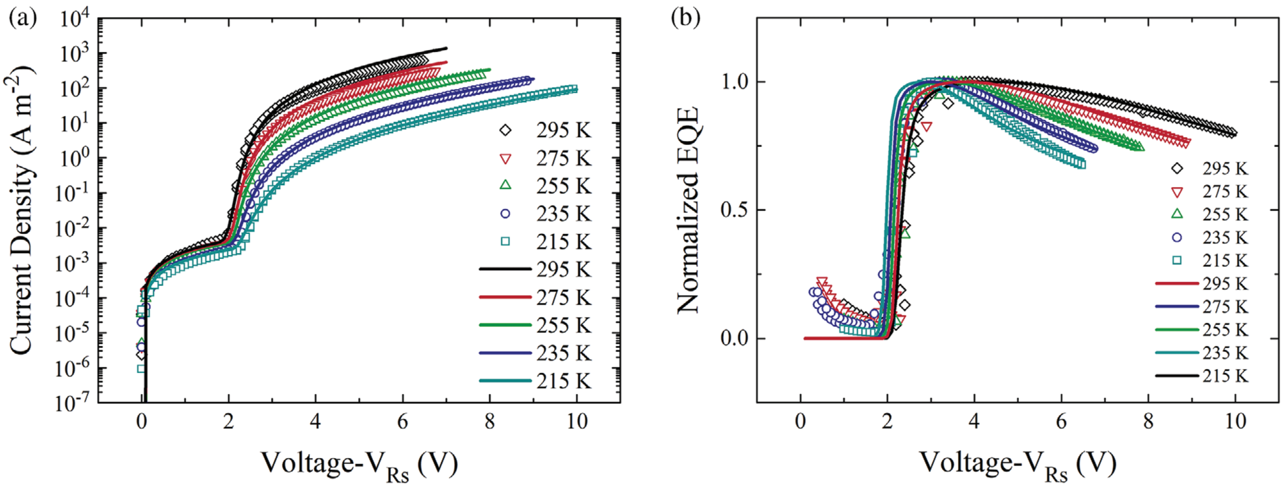

Figure 2. Temperature-dependent characterization of a 200 nm CzDBA OLED; a) Current density versus voltage corrected for the series resistance R_s of the electrodes and b) normalized EQE against voltage. The open symbols correspond to experimental data whereas the solid lines represent the simulations for various temperatures.

other two quenching processes will follow later. TTA consists of two effects that can be written as[34]

$$T_1 + T_1 \xrightarrow{3/4 * k_{TTA}} S_0 + T_1 \tag{6}$$

$$T_1 + T_1 \xrightarrow{1/4 * k_{TTA}} S_0 + S_1 \tag{7}$$

where T_1/S_1 is the triplet/singlet first excited state, S_0 is the singlet ground state, and k_{TTA} is the TTA rate constant. TTA thus reduces the triplet population and enhances the singlet population at the same time. In the rate equation, one can incorporate TTA by adding a term $+ 0.25 \cdot k_{TTA} \cdot [T(x, t)]^2$ to the differential equation for the singlet density (Equation 3) and additionally $-1.25 \cdot k_{TTA} \cdot [T(x, t)]^2$ to the differential equation for the triplet density (Equation 4). After solving these equations in steady state (Section 1 of the Supporting Information, header TTA), it leads to the full expression for the two exciton densities, given by

$$[S(x)] = \frac{0.25 \cdot \tau_s \cdot G(x) + k_{rISC} \cdot \tau_s \cdot [T(x)] + 0.25 \cdot k_{TTA} \cdot \tau_s \cdot [T(x)]^2}{1 + k_{ISC} \cdot \tau_s} \tag{8}$$

and

$$[T(x)] = -2 \frac{\tau_t^{-1} + k_{ISC} \cdot \tau_s \cdot \tau_t^{-1} + k_{rISC}}{5 \cdot k_{TTA} + 4 \cdot k_{TTA} \cdot k_{ISC} \cdot \tau_s} + \sqrt{4 \cdot \left(\frac{\tau_t^{-1} + k_{ISC} \cdot \tau_s \cdot \tau_t^{-1} + k_{rISC}}{5 \cdot k_{TTA} + 4 \cdot k_{TTA} \cdot k_{ISC} \cdot \tau_s} \right)^2 + 4 \cdot \frac{0.75 \cdot G(x) + k_{ISC} \cdot \tau_s \cdot G(x)}{5 \cdot k_{TTA} + 4 \cdot k_{TTA} \cdot k_{ISC} \cdot \tau_s}} \tag{9}$$

2.3. Validation TADF Model: Analysis of a CzDBA OLED

Inserting $[T(x)]$ into $[S(x)]/\tau_s$, dividing it by J and normalizing to the maximum then leads to the normalized OLED efficiency. The experimentally validated HO/EO parameters serve as input for the calculation of the double-carrier current density. For the calculation of the light-output, next to the conventional Langevin recombination we also include emissive SRH-recombination from traps, as well as TTA, in order to describe the voltage dependence of the efficiency. In **Figure 2**, the experimental and simulated temperature-dependent current density (Figure 2a) and efficiency (Figure 2b) as a function of voltage are presented for a 200 nm CzDBA OLED. We observe that with these processes included, the model is able to provide an excellent description of both the current–density and efficiency as a function of voltage. Since the electrical parameters were verified from single-carrier devices and the photophysical parameters were determined from a transient photoluminescence (TrPL) study, in this procedure the only fit parameter used to simulate the roll-off is k_{TTA}. In **Figure 3**, we present the fits to various emitter layer thicknesses. We find that the efficiency roll-off for all thicknesses is well described with our position-dependent model by $k_{\text{TTA}} = 7 \pm 3 \times 10^{-18}$ m^3 s^{-1}. The obtained value of k_{TTA} is comparable to values obtained for a phosphorescent emitter lightly doped in a host[21] and to values obtained from transient methods,[33,38]

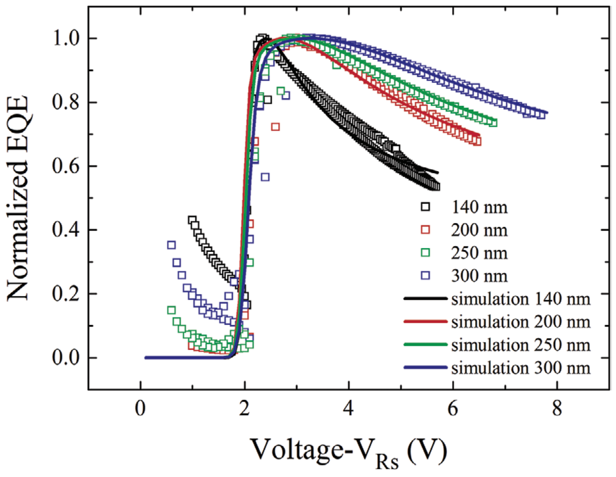

Figure 3. Normalized quantum efficiency versus voltage for different CzDBA layer thicknesses complemented by numerical simulations.

which vary typically between ≈10^{-18} and ≈10^{-19} m^3 s^{-1}. Moreover, it corresponds very well to the k_{TTA} of 8 × 10^{-18} m^3 s^{-1} found in our recent TrPL study on CzDBA.[27] Surprisingly, we find that a single k_{TTA} value fits the entire investigated temperature range (295–215 K). Recently, a kinetic Monte Carlo study of TTA in conjugated organic semiconductors found that the temperature dependence of TTA is weak in our investigated temperature range, given that the energetic disorder is small. The high mobilities of CzDBA in addition to the almost trap free transport are indicators of a low disorder and might explain the temperature independent k_{TTA} in our limited temperature range.

2.4. Comparison TADF Model to Analytical Formulas

Next to our TrPL study, we showed in a previous report that a straightforward analytical formula neglecting ISC can already provide a reasonable description of the CzDBA OLED efficiency roll-off, where the analysis of a 300 nm thick device led to a k_{TTA} of 1.5 × 10^{-17} m^3 s^{-1}, higher than obtained from our more comprehensive model in this work. The analytical formula was based on several assumptions, most notably it overlooked ISC and the position-dependent generation of the excitons and it is therefore instructive to see how these two assumptions change the fitted k_{TTA} value.

The impact of the intersystem crossing rate on k_{TTA} has been discussed in earlier work.[16] To reiterate, enhancing k_{ISC} increases the triplet population and therefore lowers the fitted k_{TTA} value, without a drastic change in the shape of the efficiency.[16] In the initial report on a host:guest system with CzDBA as emitter, a k_{ISC} of 3.8 × 10^7 s^{-1} was reported.[39] Using this k_{ISC} rate would lower k_{TTA} to a value of 1.5 × 10^{-18} m^3 s^{-1} in the analytical analysis.[16] However, a recent TrPL study done on CzDBA neat films showed that the reported k_{ISC} was overestimated since in the analysis of the PL decay annihilation processes as TTA were not incorporated.[27] Taking these processes into account a k_{ISC} of to 1 × 10^6 s^{-1} was obtained and also used in this work. To further illustrate the sensitivity of k_{TTA} to ISC and rISC we plot in Figure S3, Supporting Information the normalized efficiency versus voltage of a 300 nm OLED at 295 K for the earlier reported values of k_{ISC} as well as the currently used values obtained from PL decay. The dashed green line represents the values of k_{ISC} and k_{rISC} used in this work together with a k_{TTA} of 9 × 10^{-18} m^3 s^{-1}, which is also in very good agreement with the k_{TTA} of 8 × 10^{-18} m^3 s^{-1} obtained from PL decay measurements. Increasing k_{ISC} to 3.8 × 10^7 s^{-1} and simultaneously reducing k_{TTA} to 2.5 × 10^{-18} m^3 s^{-1} still provides still a good fit (red solid line). The same holds for k_{rISC}, where changing it from 2.2 × 10^5 to 1.1 × 10^5 s^{-1} can still provide a good fit if k_{TTA} is reduced to 2 × 10^{-18} s^{-1} (blue solid line). For comparison, the red and blue dashed lines with the correct k_{TTA}, but a different $k_{(r)ISC}$, are severely off.

Another feature that was not considered in the analytical approach is the nonuniformity of the exciton profile in the device. [16] Here, we can investigate to what extent this impacts the fitted k_{TTA} value. In phosphorescent multi-layer OLEDs, a uniform exciton profile is justified by the narrow width of the emissive layer.[33] The simulated recombination profile for a single-layer 200 nm OLED at room temperature is presented in Figure S4a (Supporting Information) and it shows that the balanced transport leads to a broadened recombination zone. Moreover, for voltages around the maximum EQE (2–3 V), it is clearly seen that the peak of the recombination profile is situated almost in the middle of the device. This is a favorable situation,[40] since it minimizes quenching of excitons at metallic contacts and a broadening of the recombination zone naturally decreases the impact of TTA. Apart from the recombination profile being slightly voltage dependent, the recombination profile of CzDBA also shifts and narrows at lower temperatures. From Table 1 we see that the disorder for holes (0.135 eV) is larger than that for electrons (0.115 eV), leading to increasingly imbalanced transport with lower temperature due to the decreased probability of thermally activated hopping at lower temperatures for holes. This is reflected in the recombination profile at 215 K which is presented in Figure S4b, Supporting Information. Because of the temperature scaling of the mobility, the current and therefore the recombination rate are naturally lower at decreased temperatures, but besides this, we also observe a shift of the recombination profile away from the anode, due to imbalanced transport. As TTA is influenced by the local density of excitons in the device, the positional dependence should play a role in the fitted k_{TTA}. This is illustrated in Figure S5, Supporting Information, where for a 200 nm device we use a uniform exciton profile for the calculation of TTA and again take k_{TTA} as a free parameter to fit the efficiency. At 295 K there is a slight change in k_{TTA} from 4 × 10^{-18} to 5 × 10^{-18} m^3 s^{-1}, whereas at 215 K we need an increased k_{TTA} of 7 × 10^{-18} m^3 s^{-1} to fit the efficiency. The overall higher k_{TTA} values when a uniform exciton profile is considered result from the fact that the uniform exciton profile lies below the peak of the position-dependent profile (Figure S4a,b, Supporting Information). Since the TTA-term in the triplet rate equation scales with the square of the triplet concentration, it results in a stronger effect of TTA when the positional dependence is considered and as such the k_{TTA} needed to fit the same roll-off is lower. When the position dependence is not included one might conclude that k_{TTA} increases with decreasing temperature, but since k_{TTA} is a diffusion dominated process this situation is not physically meaningful. This highlights the importance of using a position-dependent exciton profile, as in that case these effects are automatically taken into account.

2.5. Effect of Various Quenching Processes On the Efficiency

As a next step, we study the effect of TPQ and STA on the efficiency roll-off of the TADF OLED by analyzing the shape of the simulated efficiency curves. The derivation of the rate equations including these two other processes are also presented in Section 1 of the Supporting Information under their respective header. For TPQ we can write

$$T_1 + p/n \xrightarrow{k_{TPQ}} S_0 + p/n \tag{10}$$

where p/n refers to a hole/electron and k_{TPQ} the TPQ rate constant. The effect of TPQ is thus reducing the triplet density only.

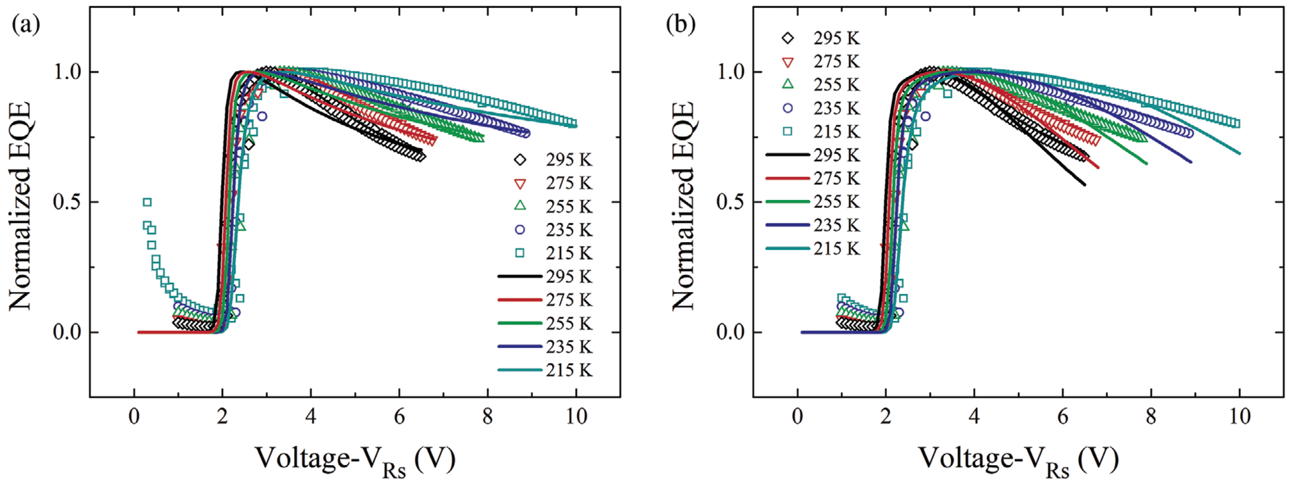

Figure 4. Temperature-dependent normalized EQE versus voltage plots for a 200 nm OLED. The open symbols correspond to the experiment, whereas the lines correspond to the simulations taking a) TPQ or b) STA as a quenching process. The values of k_{TPQ}/k_{STA} for every temperature can be found in Table 3.

STA can be written as

$$S_1 + T_1 \xrightarrow{k_{STA}} S_0 + T_1 \quad (11)$$

where k_{STA} is the singlet-triplet annihilation constant. As can be seen, STA reduces only the singlet dparensity. Two other processes that could impact the roll-off are singlet-polaron quenching (SPQ) and/or singlet-singlet annihilation (SSA). We note that the role of SSA is controversial, either being considered a significant contribution to the roll-off,[41–43] whereas other works deem SSA unimportant,[20,37] making it necessary to consider its significance in this study. In our recent TrPL study on CzDBA neat films we found that SSA was not a major decay process,[27] which justifies neglecting it in our OLED analysis. Turning our attention to SPQ, the triplet density exceeds the singlet density often by more than an order of magnitude under steady state conditions, making TPQ a far more relevant process than SPQ. Furthermore, reported rate-constants for SPQ are in the order of 10^{-20} m^3 s^{-1}.[43] Both these factors combined mean we can also neglect it in our OLED analysis.

It is observed in **Figure 4**a that the shape of the simulated efficiency with TPQ exhibits a fast drop and a subsequent flattening at higher voltage. This is contrasting with the experiment, which decreases more rapidly with increasing voltage than TPQ predicts. We lowered k_{TPQ} with decreasing temperature since it slightly improves the fitting (**Table 3**), nevertheless at all temperatures TPQ fails to reproduce the shape of the experimental efficiency. Just after V_{bi}, the number of injected carriers is high relative to the number of excitons and consequently the product of excitons and carriers can lead to a stronger roll-off than the product of two excitons, which is why TPQ shows a fast drop just after V_{bi}. At higher current densities the number of excitons surpasses the number of carriers due to the stronger scaling of excitons with the current density, $[S]/[T] \sim J$ while $n/p \sim J^{1/2}$. With this straightforward argument we can already explain why TPQ will flatten the current efficiency more than TTA. Since it does not match the voltage dependence of the experimental efficiency, it corroborates once again that TPQ is not the dominant roll-off mechanism.

In contrast to TPQ, at high current density, we see that the simulations with STA have a too strong dependence of the efficiency on voltage compared to the experiment (Figure 4b). Note that we increase the STA rate constant with temperature (Table 3) in order to improve the fit, especially in the voltages just after V_{bi}. Both TTA and STA are processes in which two excitons annihilate and to understand why they give dissimilar efficiency curves, we need to look at the fractional contributions to the efficiency in more detail. For this purpose, we chose the fit from Figure 2b at 295 K. **Figure 5** shows the various contributions to the efficiency, where we take TTA to account for the roll-off. We see that just after V_{bi} the efficiency originates to a large extent from singlets that underwent rISC, whereas at higher voltages there are growing contributions from the direct generation of singlets as well as singlets coming from TTA. Disentangling the contributions to the efficiency thus explains the flattening of the efficiency curve that we observe. The loss of triplet excitons due to TTA has its effect on the efficiency in Figure 5 implicitly via singlets coming from rISC, whose fractional contribution shrinks with increasing voltage. This highlights the importance of a fast rISC-rate once again,[44] since the mutual annihilation of triplets will be reduced if they are converted to singlets before TTA occurs. In contrast to this, STA negatively impacts the entire singlet population, meaning the

Table 3. Values of the rate constants for TPQ and STA for the investigated temperature range (the extracted rate constants correspond to the fits in Figure 4a,b).

Temperature [K]	k_{TPQ} [m^3 s^{-1}]	k_{STA} [m^3 s^{-1}]
295	3.0×10^{-18}	6.0×10^{-17}
275	2.0×10^{-18}	8.0×10^{-17}
255	1.3×10^{-18}	9.5×10^{-17}
235	9.0×10^{-19}	1.4×10^{-16}
215	6.0×10^{-19}	1.9×10^{-16}

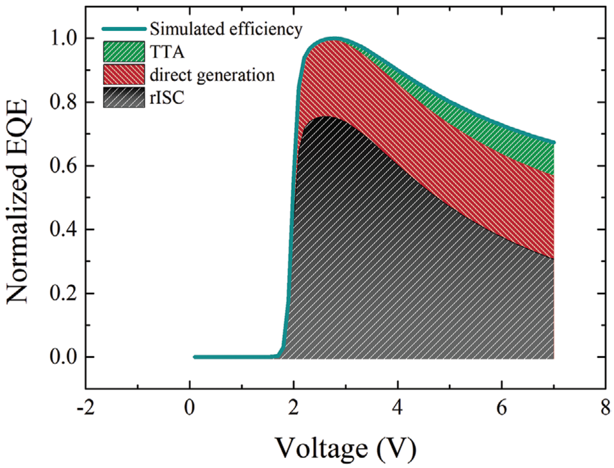

Figure 5. Normalized EQE versus voltage for a layer thickness of 200 nm showing the various contributions to the efficiency. This figure corresponds to the fit in Figure 2b at 295 K.

direct generation of singlets as well and therefore it overestimates the roll-off at higher voltage.

3. Conclusion

In summary, a device model for TADF OLEDs is presented that accurately describes the dependence of the efficiency as a function of voltage, temperature, and layer thickness. From the efficiency roll-off at higher voltages, a triplet-triplet annihilation constant of $k_{\mathrm{TTA}} = 7 \pm 3 \times 10^{-18}$ $\mathrm{m^3\ s^{-1}}$ is determined. However, for reliable extraction of the TTA constant, it is of importance that values of $k_{(\mathrm{r})\mathrm{ISC}}$ are accurately determined before as well as that the positional dependence of the exciton profile is taken into account. With our device model, we are able to discriminate between different causes for the roll-off, verifying that TTA is the dominant cause. By disentangling the various contributions to the efficiency, we elucidate why the observed voltage dependence of the roll-off cannot be due to TPQ and STA.

4. Experimental Section

In a cleanroom environment pre-patterned glass/ITO-substrates were cleaned with soap and subsequently sonicated in acetone and isopropanol for 10 min each. First, a hole injection layer (HIL) of poly(3,4-ethylenedioxythiophene):polystyrene sulfonate (PEDOT:PSS) (±40 nm) (Heraeus Clevios 4083) was spin-coated from an aqueous solution and afterwards annealed at 140 °C for 10 min. Next, $\mathrm{MoO_3}$ (6 nm), $\mathrm{C_{60}}$ (3 nm), the CzDBA active layer (different thicknesses), and TPBi (4 nm) were evaporated under a pressure of around 2×10^{-6} mbar. As cathode, we evaporated aluminium (100 nm). All evaporations were done in a glovebox environment with oxygen and water values below 0.1 ppm.

The current–voltage (*J*–*V*) measurements were carried out with a Keithley 2400 sourcemeter, while simultaneously the photocurrent–voltage measurements were carried out with a Keithley 6514 system electrometer. For the EQE measurements, a calibrated Si photodiode was used with an area larger than the emitting pixel. The device characterization was done in an inert environment ($\mathrm{O_2}$ and $\mathrm{H_2O}$ values below 0.1 ppm).

To obtain reliable simulated *J*–*V* curves, our drift-diffusion simulations employ an iterative scheme to calculate the charge carrier density with a tolerance of 1×10^{-6}, i.e., both current and charge carrier density values must converge if their values between loops vary less than the said tolerance. For stability, the iterative loop was usually repeated five times and the calculated mobility values were averaged over all iterative loops. The active layer itself was simulated using 1000 points on an exponential symmetric grid, normalized to unity. The electrical bandgap of CzDBA was determined from OLED data to be 2.8 eV and the relative permittivity was set to 3.

Supporting Information

Supporting Information is available from the Wiley Online Library or from the author.

Acknowledgements

Open access funding enabled and organized by Projekt DEAL.

Conflict of Interest

The authors declare no conflict of interest.

Author Contributions

B. v. d. Zee and Y. L. performed the experiments. B. v. d. Zee did the simulations and wrote the manuscript with input from the co-authors. G. A. H. Wetzelaer and P. W. M. Blom supervised the project.

Data Availability Statement

The data that support the findings of this study are available from the corresponding author upon reasonable request.

Keywords

device modeling, Organic light-emitting diode, thermally activated delayed fluorescence

Received: November 22, 2021
Revised: January 7, 2022
Published online: February 12, 2022

---

[1] M. A. Baldo, D. F. O'Brien, Y. You, A. Shoustikov, S. Sibley, M. E. Thompson, S. R. Forrest, *Nature* **1998**, *395*, 151.
[2] C. Adachi, M. A. Baldo, M. E. Thompson, S. R. Forrest, *J. Appl. Phys.* **2001**, *90*, 5048.
[3] K. Goushi, K. Yoshida, K. Sato, C. Adachi, *Nat. Photonics* **2012**, *6*, 253.
[4] H. Uoyama, K. Goushi, K. Shizu, H. Nomura, C. Adachi, *Nature* **2012**, *492*, 234.
[5] T. Hosokai, H. Matsuzaki, H. Nakanotani, K. Tokumaru, T. Tsutsui, A. Furube, K. Nasu, H. Nomura, M. Yahiro, C. Adachi, *Sci. Adv.* **2017**, *3*, e1603282.

[6] Z. Yang, Z. Mao, Z. Xie, Y. Zhang, S. Liu, J. Zhao, J. Xu, Z. Chi, M. P. Aldred, *Chem. Soc. Rev.* **2017**, *46*, 915.
[7] Q. Zhang, B. Li, S. Huang, H. Tanaka, C. Adachi, *Nat. Photonics* **2014**, *8*, 326.
[8] M. Y. Wong, E. Zysman-Colman, *Adv. Mater.* **2017**, *29*, 1605444.
[9] M. Kuik, G.-J. A. H. Wetzelaer, H. T. Nicolai, N. I. Crăciun, D. M. De Leeuw, P. W. M. Blom, *Adv. Mater.* **2014**, *26*, 512.
[10] D. Abbaszadeh, A. Kunz, G. A. H. Wetzelaer, J. J. Michels, N. I. Crăciun, K. Koynov, I. Lieberwirth, P. W. M. Blom, *Nat. Mater.* **2016**, *15*, 628.
[11] M. Kuik, L. J. A. Koster, A. G. Dijkstra, G. A. H. Wetzelaer, P. W. M. Blom, *Org. Electron.* **2012**, *13*, 969.
[12] Q. Niu, G. A. H. Wetzelaer, P. W. M. Blom, N. I. Crăciun, *Adv. Electron. Mater.* **2016**, *2*, 1600103.
[13] N. B. Kotadiya, P. W. M. Blom, G. A. H. Wetzelaer, *Nat. Photonics* **2019**, *13*, 765.
[14] W. Liu, N. B. Kotadiya, P. W. M. Blom, G.-J. A. H. Wetzelaer, D. Andrienko, *Adv. Mater. Technol.* **2021**, *6*, 2000120.
[15] N. B. Kotadiya, H. Lu, A. Mondal, Y. Ie, D. Andrienko, P. W. M. Blom, G.-J. A. H. Wetzelaer, *Nat. Mater.* **2018**, *17*, 329.
[16] B. van der Zee, Y. Li, G.-J. A. H. Wetzelaer, P. W. M. Blom, *Adv. Opt. Mater.* **2021**, *9*, 2100249.
[17] L. J. A. Koster, E. C. P. Smits, V. D. Mihailetchi, P. W. M. Blom, *Phys. Rev. B* **2005**, *72*, 085205.
[18] W. F. Pasveer, J. Cottaar, C. Tanase, R. Coehoorn, P. A. Bobbert, P. W. M. Blom, D. M. de Leeuw, M. A. J. Michels, *Phys. Rev. Lett.* **2005**, *94*, 206601.
[19] N. B. Kotadiya, A. Mondal, P. W. M. Blom, D. Adrienko, G. A. H. Wetzelaer, *Nat. Mater.* **2019**, *18*, 1182.
[20] K. Masui, H. Nakanotani, C. Adachi, *Org. Electron.* **2013**, *14*, 2721.
[21] S. Reineke, G. Schwartz, K. Walzer, M. Falke, K. Leo, *Appl. Phys. Lett.* **2009**, *94*, 163305.
[22] F. B. Dias, T. J. Penfold, A. P. Monkman, *Methods Appl. Fluoresc.* **2017**, *5*, 012001.
[23] H. Noda, X.-K. Chen, H. Nakanotani, T. Hosokai, M. Miyajima, N. Notsuka, Y. Kashima, J.-L. Brédas, C. Adachi, *Nat. Mater.* **2019**, *18*, 1084.
[24] T. Kobayashi, A. Niwa, K. Takaki, S. Haseyama, T. Nagase, K. Goushi, C. Adachi, H. Naito, *Phys. Rev. Appl.* **2017**, *7*, 034002.
[25] N. Haase, A. Danos, C. Pflumm, A. Morherr, P. Stachelek, A. Mekic, W. Brütting, A. P. Monkman, *J. Phys. Chem. C* **2018**, *122*, 29173.
[26] P. de Silva, C. A. Kim, T. Zhu, T. Van Voorhis, *Chem. Mater.* **2019**, *31*, 6995.
[27] K. Thakur, B. van der Zee, G.-J. A. H. Wetzelaer, C. Ramanan, P. W. M. Blom, *Adv. Opt. Mater.* **2021**, 2101784.
[28] Y. Li, N. B. Kotadiya, B. van der Zee, P. W. M. Blom, G.-J. A. H. Wetzelaer, *Adv. Opt. Mater.* **2021**, *9*, 2001812.
[29] G. A. H. Wetzelaer, M. Kuik, H. T. Nicolai, P. W. M. Blom, *Phys. Rev. B* **2011**, *83*, 165204.
[30] R. Scholz, P. Kleine, R. Lygaitis, L. Popp, S. Lenk, M. K. Etherington, A. P. Monkman, S. Reineke, *J. Phys. Chem. A* **2020**, *124*, 1535.
[31] Y. Li, L. Jiang, W. Liu, S. Xu, T.-Y. Li, F. Fries, O. Zeika, Y. Zou, C. Ramanan, S. Lenk, R. Scholz, D. Andrienko, X. Feng, K. Leo, S. Reineke, *Adv. Mater.* **2021**, *33*, 2101844.
[32] H. T. Nicolai, M. M. Mandoc, P. W. M. Blom, *Phys. Rev. B* **2011**, *83*, 195204.
[33] M. A. Baldo, C. Adachi, S. R. Forrest, *Phys. Rev. B* **2000**, *62*, 10967.
[34] C. Murawski, K. Leo, M. C. Gather, *Adv. Mater.* **2013**, *25*, 6801.
[35] S. Reineke, K. Walzer, K. Leo, *Phys. Rev. B* **2007**, *75*, 125328.
[36] R. Saxena, T. Meier, S. Athanasopoulos, H. Bässler, A. Köhler, *Phys. Rev. Appl.* **2020**, *14*, 034050.
[37] A. Niwa, S. Haseyama, T. Kobayashi, T. Nagase, K. Goushi, C. Adachi, H. Naito, *Appl. Phys. Lett.* **2018**, *113*, 083301.
[38] D. Kasemann, R. Brückner, H. Fröb, K. Leo, *Phys. Rev. B* **2011**, *84*, 115208.
[39] T.-L. Wu, M.-J. Huang, C.-C. Lin, P.-Y. Huang, T.-Y. Chou, R.-W. Chen-Cheng, H.-W. Lin, R.-S. Liu, C.-H. Cheng, *Nat. Photonics* **2018**, *12*, 235.
[40] D. E. Markov, P. W. M. Blom, *Appl. Phys. Lett.* **2005**, *87*, 233511.
[41] M. Hasan, A. Shukla, V. Ahmad, J. Sobus, F. Bencheikh, S. K. M. McGregor, M. Mamada, C. Adachi, S.-C. Lo, E. B. Namdas, *Adv. Funct. Mater.* **2020**, *30*, 2000580.
[42] H. Nakanotani, H. Sasabe, C. Adachi, *Appl. Phys. Lett.* **2005**, *86*, 213506.
[43] V. Ahmad, J. Sobus, M. Greenberg, A. Shukla, B. Philippa, A. Pivrikas, G. Vamvounis, R. White, S.-C. Lo, E. B. Namdas, *Nat. Commun.* **2020**, *11*, 4310.
[44] M. Inoue, T. Sereviius, H. Nakanotani, K. Yoshida, T. Matsushima, S. Juršnas, C. Adachi, *Chem. Phys. Lett.* **2016**, *644*, 62.